

Cite this: *Phys. Chem. Chem. Phys.*, 2013, **15**, 6726

Electron tunneling from electronically excited states of isolated bisdisulizole-derived trianion chromophores following UV absorption†

Marc-Oliver Winghart,^a Ji-Ping Yang,^{ab} Michael Kühn,^a Andreas-Neil Unterreiner,^a Thomas J. A. Wolf,^a Phuong D. Dau,^c Hong-Tao Liu,^c Dao-Ling Huang,^c Wim Klopper,^{*ad} Lai-Sheng Wang^{*c} and Manfred M. Kappes^{*ad}

Photoelectron spectra of isolated $[M\text{-BDSZ}]^{3-}$ (BDSZ = bisdisulizole, M = H, Li, Na, K, Cs) triply charged anions exhibit a dominant constant electron kinetic energy (KE) detachment feature, independent of detachment wavelengths over a wide UV range. Photoelectron imaging spectroscopy shows that this constant KE feature displays an angular distribution consistent with delayed rather than direct electron emission. Time-resolved pump-probe (388 nm/775 nm) two-colour photoelectron spectroscopy reveals that the constant KE feature results from two simultaneously populated excited states, which decay at different rates. The faster of the two rates is essentially the same for all the $[M\text{-BDSZ}]^{3-}$ species, regardless of M. The slower process is associated with lifetimes ranging from several picoseconds to tens of picoseconds. The lighter the alkali cation is, the longer the lifetime of this state. Quantum chemical calculations indicate that the two decaying states are in fact the two lowest singlet excited states of the trianions. Each of the two corresponding photoexcitations is associated with significant charge transfer. However, electron density is transferred from different ends of the roughly chain-like molecule to its aromatic center. The energy (and therefore the decay rate) of the longer-lived excited state is found to be influenced by polarization effects due to the proximal alkali cation complexed to that end of the molecule. Systematic M-dependent geometry changes, mainly due to the size of the alkali cation, lead to M-dependent shifts in transition energies. At the constant pump wavelength this leads to different amounts of vibrational energy in the respective excited state, contributing to the variations in decay rates. The current experiments and calculations confirm excited state electron tunneling detachment (ESETD) to be the mechanism responsible for the observed constant KE feature. The ESETD phenomenon may be quite common for isolated multiply charged anions, which are strong fluorophores in the condensed phase – making ESETD useful for studies of the transient response of such species after electronic excitation.

Received 2nd February 2013,
Accepted 15th March 2013

DOI: 10.1039/c3cp50497b

www.rsc.org/pccp

1. Introduction

Isolated multiply charged anions (MCAs) possess a repulsive Coulomb barrier (RCB) against electron detachment as a result of

short range attraction and long range Coulomb repulsion.^{1–3} The RCB is one of the most important characteristics of isolated MCAs and has interesting spectroscopic consequences.⁴ Under certain conditions, the RCB can even support electronic metastability of the corresponding ground state species, *i.e.* the binding energy of the excess electron is *negative*.⁵ This in turn gives rise to several interesting effects not encountered with molecules in other charge states. In particular, spontaneous tunneling autodetachment of excess electrons may be observed over timescales as long as seconds.^{6–9}

It has recently been confirmed by time-resolved studies that resonant optical absorption of MCAs can be followed by delayed tunneling detachment *from electronically excited states*, *i.e.* excited state electron tunneling detachment (ESETD).^{10–13}

^a Institute of Physical Chemistry, Karlsruhe Institute of Technology, P.O. Box 6980, 76049 Karlsruhe, Germany. E-mail: manfred.kappes@kit.edu, klopper@kit.edu, lai-sheng_wang@brown.edu

^b Hefei University of Technology, School of Sciences, Hefei 230009, People's Republic of China

^c Department of Chemistry, Brown University, Providence, Rhode Island, USA

^d Institute of Nanotechnology, Karlsruhe Institute of Technology, P.O. Box 3640, 76021 Karlsruhe, Germany

† Electronic supplementary information (ESI) available. See DOI: 10.1039/c3cp43921f

The corresponding decay lifetimes, as determined for several different isolated MCAs, were observed to be on the pico- or sub-picosecond scale, *i.e.* the tunneling rates are faster or at least comparable to all other decay channels accessible to the excited state species. The electron kinetic energies associated with ESETD are constant, independent of the detachment wavelength. They do, however, depend on the energies of the “doorway” excited states from which the tunneling occurs and on the corresponding electron affinities. Note that resonant photoexcitation in combination with ESETD was first proposed (and called “resonant tunneling”) to rationalize the relatively sharp constant kinetic energy detachment features observed in the photoelectron spectra recorded for a number of meta-stable MCAs.¹⁴

Two of the four MCAs for which ESETD dynamics has so far been quantified, the “free-base” phthalocyanine tetrasulfonate tetraanion $[\text{H}_2\text{Pc}(\text{SO}_3)_4]^{4-}$ and phenyl dibenzimidazole tetrasulfonate (bisdisulizole) $[\text{BDSZ}]^{4-}$, are *electronically metastable* in their ground states.^{10,11} It has recently been demonstrated that *electronically stable* MCAs, specifically the fluorescein and pyromethene 556 dianions, can also undergo ESETD on comparable timescales of *ca.* 1¹² and 120 ps,¹³ respectively. In all four cases, the measured electron kinetic energies are consistent with decays out of the lowest singlet excited states of the corresponding MCA chromophores. Interestingly, all four molecular MCA systems are also characterized by strong fluorescence in solution, *i.e.* the corresponding singlet excited states are comparatively long-lived. Thus it is conceivable that ESETD may be quite general for isolated MCA fluorophores. As pointed out in our recent study,¹¹ two primary conditions would have to be met for the effect to be observable in further systems. First, the parent MCAs should have a rich manifold of excited states in the visible and near ultraviolet region to facilitate the initial resonant absorption of the detachment photons. Second, the energies of the electron-emitting excited-states should lie below the corresponding RCB top, but still be close to the RCB top to ensure measurable tunneling rates. Under these conditions, the Kasha rule,¹⁵ as formulated for fluorophore light emission in the condensed phase, remains valid except that rapid electronic relaxation into a kinetic bottleneck state (typically the lowest singlet state) is followed by *electron detachment* rather than fluorescence. As a corollary, dissipation of electronic excitation in such MCAs would be routinely trackable by ESETD.

In this contribution, we explore ESETD further by probing a number of electronically stable BDSZ-based triply charged anions with systematically varying optical properties and electron binding energies. Specifically, we have examined complexes of the quadruply charged BDSZ^{4-} anion with one singly charged cation, $[\text{M-BDSZ}]^{3-}$ ($\text{M} = \text{H}, \text{Li}, \text{Na}, \text{K}, \text{Cs}$), as well as a more strongly perturbed BDSZ derivative, in which one of the four terminal sulfonates (negative charge carriers) is replaced by a hydrogen atom, *i.e.* $[\text{BDSZ-SO}_3 + \text{H}]^{3-}$. Questions that we are interested in include: what constitutes “close enough to the RCB maximum” for ESETD to be observable and what happens when multiple tunneling states are encountered? By means of velocity map imaging photoelectron spectroscopy (VMI-PES),

time-resolved pump-probe photoelectron spectroscopy (TR-PES), as well as quantum chemical calculations of the corresponding ground and excited states, we find that all of these species show strong ESETD following UV photoexcitation. The corresponding state lifetimes all fall in the ps to tens of ps range. Complexes with smaller alkali ions have longer lifetimes. We rationalize these trends in alkali size in terms of the variations in the corresponding excited state energies and also discuss the observed lifetimes in terms of the timescale of electronic to vibrational energy redistribution in these isolated MCA systems.

2. Methods

2.1 Experimental methods

$\text{Na}_2\text{H}_2\text{-BDSZ}$ (Disodium Phenyl Dibenzimidazole Tetrasulfonate (or Disodium Bisdisulizole)), an organic chromophore with large near UV absorption cross section, was obtained from Symrise. Mass and charge selected ion beams were generated using electrospray ionization as previously described.¹¹ Briefly, $[\text{Na-BDSZ}]^{3-}$ and $[\text{H-BDSZ}]^{3-}$ anions were generated by electrospray of a 2 mM solution of $\text{Na}_2\text{H}_2\text{-BDSZ}$ dissolved in a mixture of water and methanol. $[\text{M-BDSZ}]^{3-}$ ($\text{M} = \text{Li}, \text{K}, \text{Cs}$) were obtained by adding the corresponding alkali halide to the Na-BDSZ stock solution. $[\text{BDSZ-SO}_3 + \text{H}]^{3-}$, *i.e.* the parent species with a sulfonate group replaced by a hydrogen atom ($= \text{C}_{20}\text{H}_{11}\text{N}_4\text{S}_3\text{O}_9^{3-}$), was observed in small abundances among the ions generated by electrospray from $\text{Na}_2\text{H}_2\text{-BDSZ}$ solutions under standard conditions. The stoichiometric composition of this species was confirmed by high resolution mass spectrometry using an LTQ Orbitrap instrument at KIT. This analysis also shows that <6% of the total $[\text{BDSZ-SO}_3 + \text{H}]^{3-}$ ion signal is comprised of a contaminant radical species $[\text{BDSZ-SO}_3]^{3-}$ differing by one hydrogen mass. We suspect that the corresponding desulfonated species are already present in the solution.

The single-photon PES experiments carried out at Brown University were done using both a magnetic-bottle PES apparatus¹⁶ and a VMI-PES setup¹⁷ under both room temperature and low temperature conditions.^{18,19} The magnetic-bottle-based TR-PES at KIT was used for the two-colour, two-photon transient PES experiments at room temperature.^{10,20}

2.1.1 Velocity map imaging photoelectron spectroscopy. The velocity-map imaging system at Brown was adapted in our electrospray PES apparatus¹⁶ by replacing the original magnetic-bottle photoelectron analyzer. Details of the modifications have been described previously.¹⁷ Anions were accumulated in a Paul-type ion trap and mass was selected using a time-of-flight mass spectrometer. The desired anions were directed to the center of the photoelectron imaging system, where they were detached by a linearly polarized laser beam from a Nd/YAG laser at two wavelengths: 266 nm (4.661 eV) and 355 nm (3.496 eV). The nascent electron cloud was accelerated by a high voltage pulse applied to the imaging electrodes and was projected onto a phosphor screen behind a set of micro-channel plates (MCPs). The positions of the photoelectrons on the phosphor screen were recorded using a charge-coupled-device (CCD) camera and accumulated as a photoelectron image.

The laser polarization was parallel to the surface of the MCP and the phosphor screen detector, so that the original shape of the 3D electron clouds could be rebuilt through inverse Abel transformation from the recorded 2D images.²¹

Depending on the desired experiments, we can switch between VMI-PES and magnetic-bottle PES. The VMI-PES system can provide photoelectron angular distribution information, but the signal to noise ratios are poor at high photon energies. The magnetic-bottle photoelectron analyzer can record relatively good photoelectron signals even at very high photon energies, *i.e.* 206 nm from a dye laser or 157 nm from an F₂ excimer laser. In both the magnetic-bottle PES and VMI-PES experiments, the electron kinetic energy (KE) resolution ($\Delta KE/KE$) is $\sim 3\%$ for electrons around 1 eV, as was calibrated by the known spectra of Br[−], I[−], and Au[−]. Br[−] and I[−] can be easily prepared by the corresponding alkali halide solution, while Au[−] was generated by electrospray of a solution of PPh₃AuCl and NaSCH₃ (~ 1 mM) in acetonitrile containing a trace amount of methanol.²² In addition, we have modified our first generation ESI-PES apparatus with an cryogenically cooled Paul trap,¹⁸ which can reach down to 4.4 K.¹⁹ In the current work, experiments were carried out at an ion trap temperature of 20 K.

2.1.2 Time resolved pump–probe photoelectron spectroscopy. The TR-PES system at KIT comprised an electrospray source and a magnetic-bottle spectrometer as described previously.^{10,19} As in our previous time-resolved studies on other negatively charged anions,^{10,11} femtosecond laser pulses were provided by an Er³⁺ fiber oscillator and a regenerative Ti:sapphire amplifier operating at a 1 kHz repetition rate (Clark-MXR, CPA 2001). After frequency-doubling of the 775 nm fundamental output in an appropriately cut 0.1 mm thick BBO crystal (β -barium borate), pump pulses at 388 nm and probe pulses at 775 nm were available with a pump–probe time resolution of roughly 440 ± 30 fs (as determined by cross-correlation measurements of pump and probe laser beams).¹¹ Pulse energies were typically on the order of 100 μ J for the fundamental (probe) and about 20 μ J at 388 nm (pump). Pump and probe pulses with parallel polarization were delayed relative to each other using a computer controlled optical delay line (Nanomover, Melles Griot). For certain one-photon measurements, we also used frequency-tripled fundamental at 258 nm with pulse energies of 20 μ J. The ion beam experiment was run synchronously with the laser system (at 1 kHz). This was achieved by accumulating the output of the electrospray ion source in a cylindrical rf ion trap prior to pulsed extraction into a linear time-of-flight mass spectrometer. The pulse decelerated anions interacted with the unfocused pump and probe laser beams in the detachment chamber of the magnetic-bottle photoelectron spectrometer. Photoelectron spectra were calibrated against the known spectrum of IrBr₆^{2−}.²³ The electron kinetic energy resolution ($\Delta KE/KE$) of the TR-PES apparatus was $\sim 5\%$ for KE ~ 1 eV.

2.2 Theoretical methods

Several model systems were investigated theoretically by means of quantum chemical computations (see Section 4.1). All of these computations were carried out in the framework of

density functional theory (DFT) for ground states and time-dependent density functional theory (TDDFT) for electronically excited states.²⁴ For these DFT and TDDFT computations, we used the B3LYP functional²⁵ in conjunction with the def2-SVPD basis set.²⁶ The use of a hybrid functional such as B3LYP was considered important in view of the multiple negative charges and the distinct charge-transfer character of the excited states. For the same reason, it was considered important to use a basis set with diffuse functions,²⁷ such as those provided by the def2-SVPD basis set. All computations were performed using the Turbomole program system,²⁸ version 6.4. All computations were performed using quadrature grid m4, self-consistent field convergence threshold scfconv = 9, density convergence threshold denconv = 1d-8 and TDDFT convergence threshold rpaconv = 6. Geometry optimizations were performed with the options energy 8 and gcart 6 as thresholds for the total energy and the Cartesian gradient, respectively.

3. Results

3.1 Velocity map imaging and magnetic-bottle PES experiments (one-photon detachment)

Fig. 1 provides an overview of the VMI-PES results for two prototypical [M-BDSZ]^{3−} systems, M = Na and H, measured at 266 and 355 nm. At 266 nm, for both trianions, two detachment features are observed and labeled X and T_a. The X band is broad and relatively weak, whereas the T_a band is sharper and more intense. Because of the RCB present in MCAs, the higher binding energy T_a band is expected to be cut off at 355 nm.^{2–4} However, the band observed at 355 nm for both trianions is not the expected X band, but rather it resembles the T_a band in both cases. In fact, the band observed at 355 nm has the same electron kinetic energy as the T_a band in the 266 nm spectrum. The spectral features and photon-energy dependent behaviour of the two [M-BDSZ]^{3−} trianions are similar to those of the parent [BDSZ]^{4−} tetraanion.¹¹ To understand the nature of the constant kinetic energy feature, we measured PES spectra of the two trianions over a wide photon energy range from 412 nm to 206 nm, as shown in Fig. 2 and plotted on the kinetic energy scale. The 355 nm and 266 nm spectra recorded using both the VMI and magnetic-bottle methods agree with each other. The constant kinetic energy features labeled as T_a are shown more clearly in Fig. 2. In fact, this feature is present in the spectra at all detachment wavelengths. For [Na-BDSZ]^{3−}, a second constant kinetic energy feature is also observed at lower kinetic energies (T_b in Fig. 2a). This feature is discernible in the VMI-PES spectra as a shoulder on the higher binding energy side of the T_a band (Fig. 1), due to the slightly poorer energy resolution for high kinetic energy electrons in the VMI method. Apart from the constant kinetic energy features, additional photoelectron signals are observed in the 206 nm spectra with electron kinetic energies scaling linearly with the photon energy. These features are due to direct photodetachment from deeper molecular orbitals of the trianions.

The photoelectron angular distributions (recorded at room temperature) provide further insight. The constant kinetic

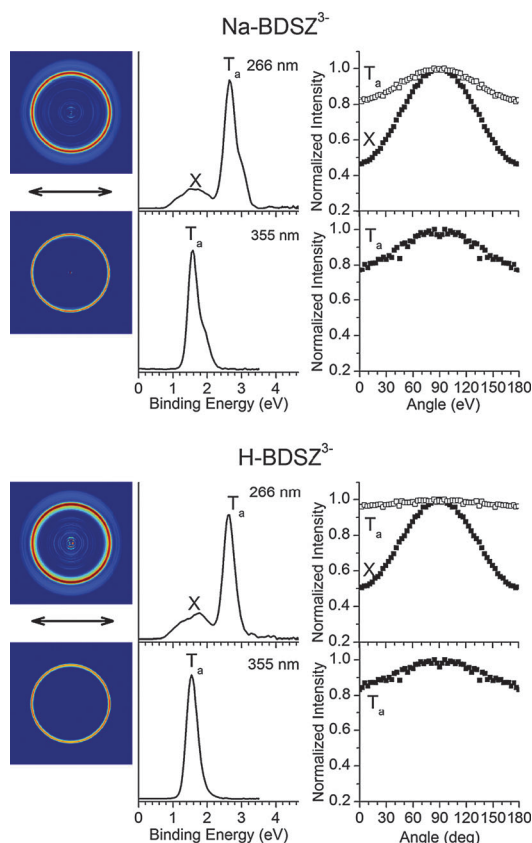


Fig. 1 Single-photon VMI-PES results for $[\text{H-BDSZ}]^{3-}$ and $[\text{Na-BDSZ}]^{3-}$ at 355 nm and 266 nm. Shown are the photoelectron images, the photoelectron spectra plotted versus electron binding energies, and the electron angular distributions for the two observed spectral bands. The electron angular distributions quantify the photoelectron image intensities. They are normalized to one corresponding to the intensity maximum for each transition. Because of symmetry, only the top half of the image is plotted from 0 to 180 degrees in each case.¹⁷

energy photoelectron features display roughly isotropic angular distributions, indicating that the corresponding photoelectrons are emitted on a time scale comparable or longer than that required for rotational averaging. On the other hand, the *X* band, which is due to direct detachment, shows strong anisotropy, suggesting that direct photodetachment occurs on a timescale much shorter than the rotational period of the ion in question.

As shown in Fig. S2 in the ESI,[†] varying the temperature of the entrance capillary (one of the electrospray conditions), so as to yield ions with lower vibrational excitation closer to room temperature, leads to simplification of the $[\text{Na-BDSZ}]^{3-}$ photoelectron spectra. The second constant energy detachment feature (T_b) is no longer observed. This shows that for $[\text{Na-BDSZ}]^{3-}$ there are two different conformers with slightly different free energies, which can be populated at elevated electrospray source temperatures. Under electrospray conditions near room temperature, only one conformer (corresponding to T_a) is generated. Similar phenomena were observed for $[\text{M-BDSZ}]^{3-}$, $\text{M} = \text{Li}$ and K , but not for $\text{M} = \text{H}$ which always shows only one conformer.

Note also that, when “hot-sprayed” $[\text{Na-BDSZ}]^{3-}$ and $[\text{H-BDSZ}]^{3-}$ ions were captured in the ion trap at either room

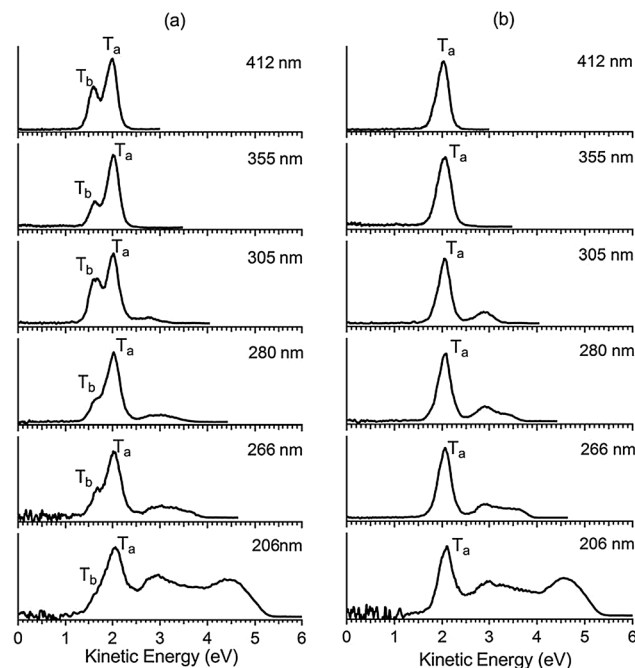


Fig. 2 Single-photon magnetic bottle-PES data for (a) $[\text{Na-BDSZ}]^{3-}$ and (b) $[\text{H-BDSZ}]^{3-}$ at different photon energies, plotted versus electron kinetic energy. Note the constant kinetic energy features (T_a/T_b) independent of detachment wavelengths (see also Fig. 1).

temperature or cryogenic temperature (20 K), $[\text{Na-BDSZ}]^{3-}$ continued to show the occurrence of both conformers whereas $[\text{H-BDSZ}]^{3-}$ always manifested only one conformer (see also Fig. S4 in the ESI[†]). This confirms that the higher free energy conformers for $[\text{M-BDSZ}]^{3-}$ ($\text{M} = \text{Li}$, Na and K) are formed in the electrospray source not during anion trapping.

All further measurements from KIT described in this paper were performed under electrospray conditions yielding only the lower free energy conformers (corresponding to T_a).

From the single-photon PES measurements performed at 258 nm detachment wavelength, we were able to determine adiabatic electron detachment energies (ADEs) for all (single conformer) MCA species studied here. The procedure used to obtain this quantity has been previously described.²⁹ For all $[\text{M-BDSZ}]^{3-}$ ($\text{M} = \text{Li}$, Na , K , Cs) and $[\text{H-BDSZ}]^{3-}$, the corresponding values were the same within our experimental accuracies: $\text{ADE} = 0.8 \pm 0.1$ eV as determined for the broad band at low binding energy (*i.e.*, the *X* band in Fig. 1). The ADE of $[\text{BDSZ-SO}_3 + \text{H}]^{3-}$ was measured to be 0.5 ± 0.1 eV. As typical examples, Fig. S3 (ESI[†]) shows the 258 nm one-colour PES measurements for $[\text{K-BDSZ}]^{3-}$ and $[\text{BDSZ-SO}_3 + \text{H}]^{3-}$, plotted on the kinetic energy scale. In all trianion cases studied here, we estimate the RCB heights (as measured from the spectral cutoff for the direct detachment features) to be ~ 2.5 eV.

According to our mechanistic picture (see below), integrated ESETD signal intensities are a measure of (unknown) absorption cross sections, photon fluxes, tunneling rates and also of the rates of other competing decay processes (primarily internal conversion). We have not attempted to quantitatively compare the absolute intensities of the tunneling signals among all the MCAs.

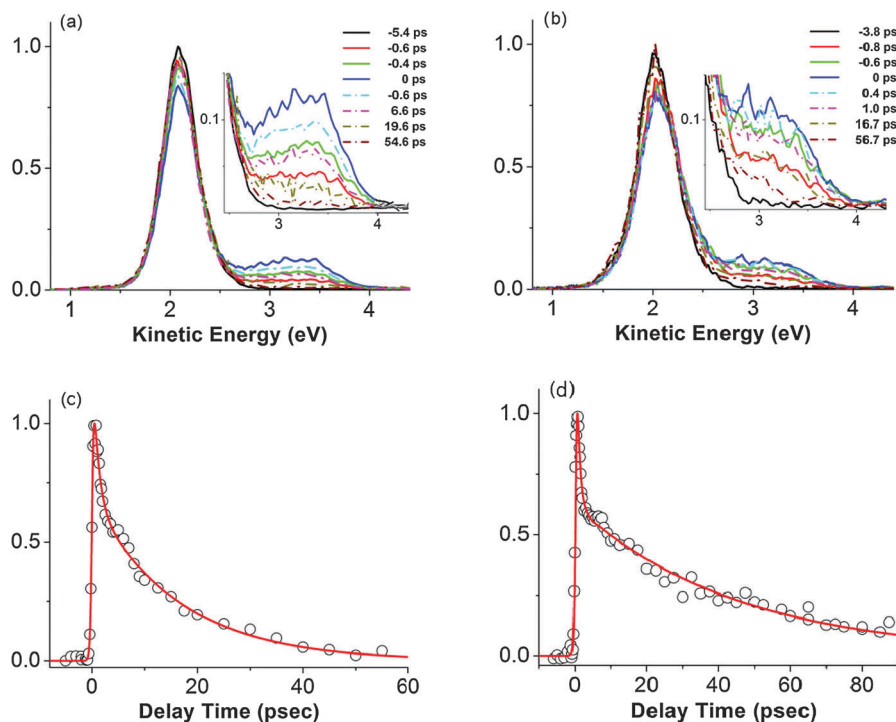


Fig. 3 Time resolved PES measurements at 388 nm pump and 775 nm probe. (a) and (b) provide overviews of the PE-spectra for $[\text{H-BDSZ}]^{3-}$ and $[\text{Li-BDSZ}]^{3-}$, respectively, showing the constant kinetic energy detachment feature and two-photon transients in the 2.6–4.0 eV range vs. pump–probe delay; (c) and (d) compare integrated transient signals (open circles) vs. pump–probe delays with a superimposed kinetic model (see the text for details).

Nevertheless, within a factor of about 5 we observed that the integrated one-photon tunneling signal, induced upon 388 nm irradiation, was independent of M (M = H, Li, Na, K, Cs), with everything else held constant.

3.2 Time-resolved pump–probe PES measurements

Fig. 3a and b, for $[\text{H-BDSZ}]^{3-}$ and $[\text{Li-BDSZ}]^{3-}$, respectively, show the results of TR-PES measurements upon exciting with a 440 ± 30 fs laser pulse at 388 nm and probing with a second 775 nm fs pulse at a variety of delay times. At purely one photon (pump pulse) absorption of 388 nm radiation (*cf.* Fig. 1 and 2, and Fig. S2, ESI†), only photoemission of electrons at a constant kinetic energy of ~ 2.1 eV is observed. Superposition of a second fs laser pulse at 775 nm within a sufficiently short time delay after the pump pulse leads to the generation of additional higher kinetic energy photoelectrons (corresponding to a two-photon detachment response). Integrating this transient photoelectron signal within the kinetic energy interval 2.6–4.0 eV leads to the pump–probe transient time-dependencies shown in Fig. 3c and d. These were modelled by fitting two parallel first order decay processes (for each of the two excited subpopulations), yielding best fit time constants τ_1 and τ_2 as shown in Table 1.

Analogous measurements with the same pump–probe wavelengths were carried out for all other $[\text{M-BDSZ}]^{3-}$ systems considered here. The corresponding data are shown together in Fig. 4. Again we modelled the data with two parallel first order decays, yielding best fits as indicated by the superimposed continuous lines (Table 1). Note the systematic trends

in the lifetimes: the heavier the alkali cation the shorter the τ_2 value. In contrast, the first (fast) time constant is, within our experimental accuracy, practically invariant for all the trianions. Interestingly, the proton does not follow the overall trend: its τ_2 lies intermediate between that of M = Na and K. Additionally, it is noteworthy that the relative weights of τ_1 versus τ_2 decay contributions (also part of the three-parameter kinetic fits) remain roughly constant throughout the series at *ca.* 60 : 40%.

As indicated in Section 2.1, we have also probed the desulfonated trianion derivative species $[\text{BDSZ-SO}_3 + \text{H}]^{3-}$, as shown in Fig. 5. Modeling the data with two-parallel first order decays as was done for the other trianions results in $\tau_1 = 0.9 \pm 0.4$ and $\tau_2 = 4.9 \pm 2$ ps. In contrast to the $[\text{M-BDSZ}]^{3-}$ systems, the relative weights of the τ_1 vs. τ_2 decay were 90 : 10 (Table 1).

Table 1 Lifetimes derived from fs pump–probe PES, assuming two parallel first order decays for all trianion species. Also shown are the relative weights of the two decay processes, which provide the best fits to the measured transients

System	Lifetime τ_1 (ps)	Lifetime τ_2 (ps)	Weighting ^a $A_2/(A_1 + A_2)$ (%)
H-BDSZ ³⁻	1.0 ± 0.4	16.1 ± 2.5	49 ± 3
Li-BDSZ ³⁻	0.8 ± 0.4	45 ± 5	38 ± 5
Na-BDSZ ³⁻	1.2 ± 0.4	29 ± 3	42 ± 3
K-BDSZ ³⁻	0.6 ± 0.4	8.2 ± 1.5	38 ± 5
Cs-BDSZ ³⁻	1.0 ± 0.4	5.8 ± 1	37 ± 5
BDSZ-(SO ₃ + H) ³⁻	0.9 ± 0.4	4.9 ± 2	10 ± 3

^a A_1 and A_2 are constants determining the weighting of the two parallel relaxation channels associated with τ_1 and τ_2 in the fitting function.

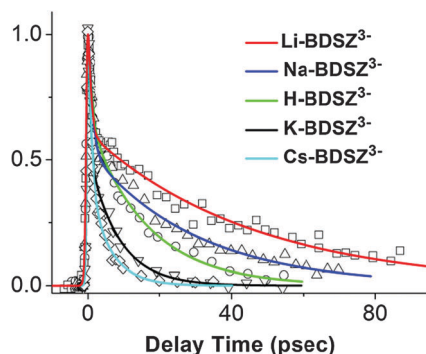


Fig. 4 Two-photon TR-PES of $[M\text{-BDSZ}]^{3-}$, $M = \text{H, Li, Na, K, Cs}$, at 388/775 nm. Shown are the transients determined from the respective photoelectron spectra by plotting the two-photon signal integrated over the electron kinetic energy range 2.6–4.0 eV (open symbols) versus the pump–probe delay. The superimposed continuous lines are best fits of a parallel decay model.

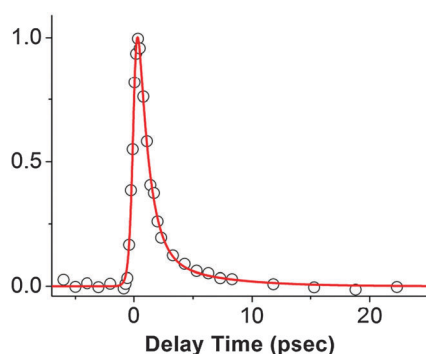


Fig. 5 Two-photon TR-PES of $[\text{BDSZ-SO}_3 + \text{H}]^{3-}$ at 388/775 nm. Shown are the transients determined from the respective photoelectron spectra by plotting the two-photon signal integrated over the electron kinetic energy range 3.0–4.4 eV (open circles) versus the pump–probe delay.

To take into account the possibility of other decay channels we have also attempted to fit the transients using more complicated kinetic models. In all cases, the fits obtained using the parallel single exponential decay model were significantly better.

Note that in all trianion systems for which we have studied this quantitatively, pump + probe irradiation was seen to lead to significant depletion of the 2.1 eV constant kinetic energy PE feature observed upon purely pump irradiation. Fig. S4 (ESI†) demonstrates this for $[M\text{-BDSZ}]^{3-}$ ($M = \text{H, Li and Na}$) as well as for $\text{BDSZ}(\text{-SO}_3 + \text{H})^{3-}$ at the maximum temporal overlap of pump and probe pulses. Fig. 3 presents more extensive measurements at a variety of time delays for $[\text{H-BDSZ}]^{3-}$ and $[\text{Li-BDSZ}]^{3-}$. These show that the depletion time-dependence matches that of the fast photoelectron transient. Consequently, the population of a common excited state(s) is being probed: (i) by pump + probe photodetachment (to yield high energy photoelectrons) and (ii) by complementary depletion of the constant kinetic energy PE feature. Note that for the measurements shown in Fig. S4 (ESI†), the ratio of integrated depletion to transient pump–probe signal intensities is always nearly one. The simplest explanation of this is that almost all pump

photoexcited trianions decay by loss of “constant kinetic energy” photoelectrons. We will return to this point below.

4. Discussion

Solutions of $\text{Na}_2\text{H}_2\text{-BDSZ}$ dissolved in polar solvents show a strong, broad UV absorption feature centered at 340 nm. Furthermore, the molecule fluoresces with a corresponding Stokes shift of 50 nm as can be seen in Fig. S1 (ESI†) which shows the solution absorption and fluorescence spectra. Hence, for all the BDSZ-based gaseous MCAs, we also expect strong UV absorption cross sections in the wavelength range of interest here – as also supported by TDDFT calculations (see below).

In a recent publication, we have reported the TR-PES response of $[\text{BDSZ}]^{4-}$ subject to 388 nm pumping and 775 nm probing.¹¹ In addition to a constant electron kinetic energy feature at ~ 4.0 eV (already observed upon one photon irradiation), a transient two-photon signal was observed with a lifetime of *ca.* 500 fs. We rationalized this as corresponding to the lifetime of the lowest singlet excited state of the chromophore. In the gas phase, this lowest singlet excited state decays predominantly by two processes: (i) internal conversion to the ground state and (ii) *excited state electron tunneling detachment (ESETD)* through the RCB. Fluorescence, a significant decay process following UV excitation of BDSZ in the condensed phase, was deemed not to play a significant role because the observed subpicosecond lifetimes were orders of magnitude shorter than the radiative lifetime expected for such a chromophore. Inter-system crossing was also ruled out as significantly contributing to the observed photoexcited tetraanion decay rate based on an estimate of the relative energies of the lowest singlet and triplet states (the lowest triplet state is significantly lower in energy than the lowest singlet excited state (see also below)).

The BDSZ-based trianion adducts/derivatives considered here also show a constant kinetic energy feature in their one-photon photoelectron spectra independent of detachment wavelengths (Fig. 1 and 2). This, together with the corresponding VMI- and TR-PES measurements, indicates that significant ESETD also occurs in these systems. In order to rationalize the systematic trends in the decay rates as a function of the complexed ion, we next model the corresponding ground and excited states *via* (time-dependent) density functional theory.

4.1 Theoretical description of the ground and electronically excited states

4.1.1 The model system $[\text{BDSZ}]^{2-}$. DFT calculations on the quadruply charged system $[\text{BDSZ}]^{4-}$ are not meaningful due to the very high negative charge and the unbound electrons in the calculations.³⁰ Such calculations were therefore not performed. Rather, for our DFT computations, we have considered a model system in which the two sulfonate groups that are located at *one end* of the molecule have been removed and replaced by hydrogen atoms. This model system is a *doubly charged* anion with only negative occupied orbital energies at the B3LYP/def2-SVPD level.

The model is denoted $[\text{BDSZ}]^{2-}$, where the prime indicates that two sulfonate groups have been removed. Fig. 6 shows the B3LYP/def2-SVPD optimized geometries of two isomers of this model system (both exhibit C_s symmetry). At this level of theory, the electronic energy of the isomer shown in the upper part of Fig. 6 lies 62 kJ mol^{-1} below the isomer in the lower part, due to the formation of a $\text{N-H}\cdots\text{O}^-$ hydrogen bond. The Mulliken charge on the respective O atom is much more negative ($-1.026e$) [and on the respective N atom much more positive ($0.640e$)] than on the other O [N] atom. Due to the stabilization of the sulfonate group involved in the $\text{N-H}\cdots\text{O}^-$ hydrogen bond, the HOMO is located on the other end of the two sulfonate groups. Accordingly, the HOMOs of the two isomers are located on different sulfonate groups. The B3LYP/def2-SVPD electronic energy of the most stable isomer (upper panel of Fig. 6) is $E = -2234.0546E_h$. The energies of the frontier orbitals are $\epsilon_{\text{HOMO}} = -0.45 \text{ eV}$ and $\epsilon_{\text{LUMO}} = 1.53 \text{ eV}$. At the B3LYP/def2-SVPD level, the first singlet excited state (S_1) is found at 1.68 eV . This is an $^1A'$ state with 99.4% HOMO–LUMO character. Fig. 6 also contains plots of these HOMO and LUMO orbitals – indicating that the corresponding transition is of a charge-transfer type.

In view of the charge-transfer character of the excited state, notably of a doubly charged anion, we do not expect the B3LYP functional to provide reliable excitation energies in an absolute sense.³¹ In the following, therefore, we focus on the ground-state equilibrium geometries and the frontier orbitals of a series of model compounds.

4.1.2 The protonated model system $[\text{H-BDSZ}]^-$. Protonation of the model system $[\text{BDSZ}]^{2-}$ may occur at both sulfonate groups of the two isomers shown in Fig. 6. This gives rise to four isomers for $[\text{H-BDSZ}]^-$ (Fig. 7).

One may expect the isomer “up–down” (“ud”) to be lowest in energy, because here the $\text{N-H}\cdots\text{O}^-$ hydrogen bond of the dianion $[\text{BDSZ}]^{2-}$ is left intact. This is confirmed by the DFT computations. The equilibrium geometries of the four isomers

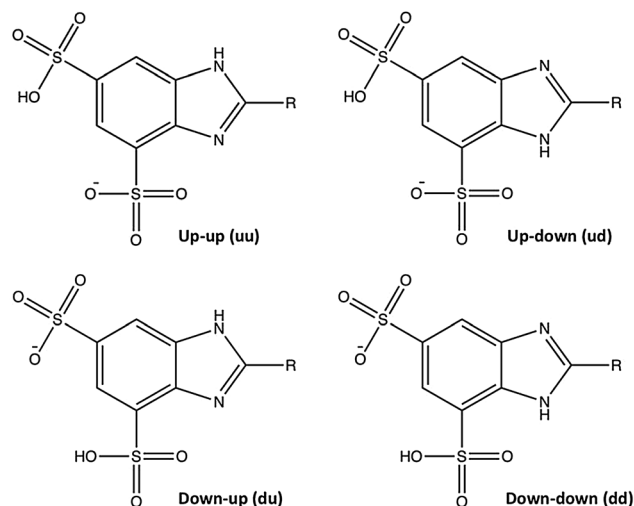


Fig. 7 Four isomers of the model system $[\text{H-BDSZ}]^-$. R is the remainder of the system.

were optimized at the B3LYP/def2-SVPD level and the total electronic energies are given in Table 2, together with the energies of the frontier orbitals as well as the singlet and (significantly lower lying) triplet vertical excitation energies. The isomer “ud” has by far the lowest total energy, 36 kJ mol^{-1} below the isomer “du”.

Interestingly, the HOMO of the dianion $[\text{BDSZ}]^{2-}$ is stabilized considerably by the protonation, and therefore, in the $[\text{H-BDSZ}]^-$ system, the HOMO is located on the sulfonate group involved in the $\text{N-H}\cdots\text{O}^-$ hydrogen bond. The Mulliken charges on the N and O atoms in this bond are 0.664 and $-1.006e$, respectively, which are values not very different from those for the most stable dianion in Fig. 6 (top). Hence, the hydrogen bonds in the most stable isomers of $[\text{BDSZ}]^{2-}$ and $[\text{H-BDSZ}]^-$ are very similar. This is not true for the “dd” isomer of $[\text{H-BDSZ}]^-$, where the hydrogen-bonding sulfonate group is protonated, which results in a significant weakening of the hydrogen bond.

4.1.3 DFT results for $[\text{M-BDSZ}]^-$ with $\text{M} = \text{Li}, \text{Na}, \text{K}, \text{Rb}, \text{Cs}$. When an alkali cation is added instead of a proton, the resulting structure is *quite different*. A geometry optimization at the B3LYP/def2-SVPD level revealed that the alkali ion takes a position between the two sulfonate groups, as illustrated in Fig. 9.

Fig. 10 provides a side view of the molecule with the two sulfonate groups, showing that the alkali ion is located above

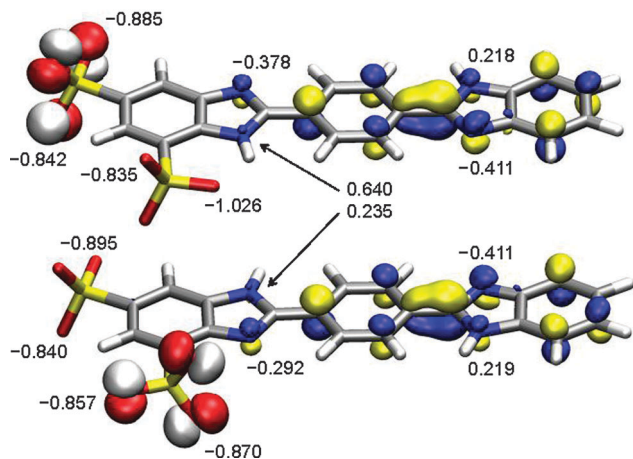


Fig. 6 Two isomers of the model system $[\text{BDSZ}]^{2-}$. Shown are the HOMO (red/white) and LUMO (blue/yellow) of each isomer together with the Mulliken charges (in units of e) at the O and N atoms, as obtained at the B3LYP/def2-SVPD level. Both isomers exhibit C_s symmetry.

Table 2 Ground-state energies (GSE in E_h) of four isomers of the model system $[\text{H-BDSZ}]^-$, together with vertical excitation energies (VEE in eV) at the B3LYP/def2-SVPD level. Also given are the HOMO and LUMO orbital energies, in eV

	Up-up (uu)	Up-down (ud)	Down-up (du)	Down-down (dd)
GSE, S_0	−2234.6216	−2234.6486	−2234.6350	−2234.6323
E_{LUMO}	−0.46	−0.37	−0.83	−0.58
E_{HOMO}	−2.83	−3.55	−3.08	−2.98
VEE, S_1	1.94	2.78	1.89	2.04
VEE, S_2	2.80	3.25	2.67	2.79
VEE, T_1	1.93	2.43	1.88	2.04

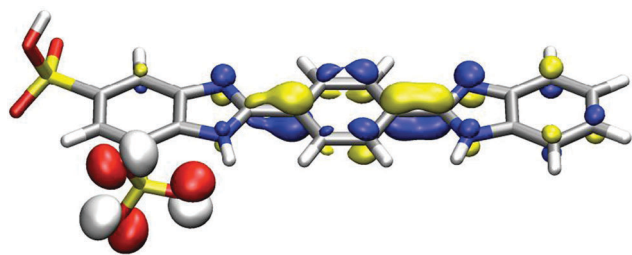


Fig. 8 Low-lying "ud" isomer of the model system $[H-BDSZ']^-$. Shown are the HOMO (red/white) and LUMO (blue/yellow) frontier orbitals as obtained at the B3LYP/def2-SVPD level.

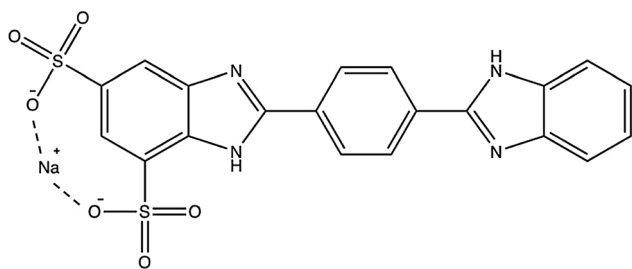


Fig. 9 Model system $[Na-BDSZ']^-$.

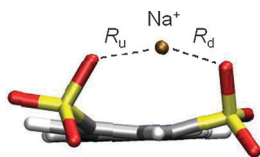


Fig. 10 Position of the Na^+ ion in $[Na-BDSZ']^-$ as obtained at the B3LYP/def2-SVPD level. Indicated are two O–Na distances. R_d is the distance to the sulfonate group involved in the $N-H\cdots O^-$ hydrogen bond.

the molecular plane and that the sulfonate groups are bent towards it. The two $M^+\cdots O^-$ distances of $[M-BDSZ']^-$ are given in Table 3 for $M = Li, Na, K, Rb, Cs$. Obviously, both distances become larger with increasing nuclear charge and ion radius. Apparently, smaller distances lead to stronger Coulombic interactions and hence to a larger HOMO–LUMO gap. Accordingly, the vertical excitation energies increase in the series from $Cs \rightarrow Rb \rightarrow K \rightarrow Na \rightarrow Li$. A similar trend is observed for the binding energy of the cation. It is largest for Li and smallest for Cs (Table 3). We emphasize that the proton adduct *behaves differently* due to the formation of an –OH group.

Table 3 Binding energies (D_e) and $M^+\cdots O^-$ distances of the model system $[M-BDSZ']^-$, in comparison with the energy of the deprotonation reaction $[H-BDSZ']^- \rightarrow [BDSZ']^{2-} + H^+$. Also shown are the HOMO–LUMO gap and the first singlet (S_1) vertical excitation energy (VEE) at the B3LYP/def2-SVPD level

Alkali ion	D_e (kJ mol $^{-1}$)	R_u (pm)	R_d (pm)	Gap (eV)	VEE (eV)
Li^+	884	185.6	187.0	3.50	3.18
Na^+	788	221.4	225.4	3.47	3.14
K^+	704	264.4	279.9	3.36	3.03
Rb^+	670	280.9	294.7	3.31	2.98
Cs^+	643	297.1	308.6	3.29	2.96
$[H-BDSZ']^-$	1560			3.19	2.78

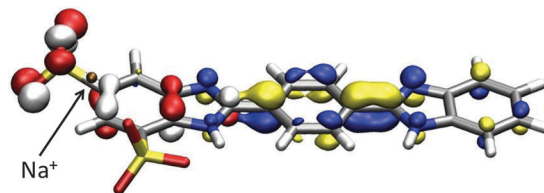


Fig. 11 HOMO (red/white) and LUMO (blue/yellow) frontier orbitals of the $[Na-BDSZ']^-$ model system as obtained at the B3LYP/def2-SVPD level.

Fig. 11 shows the HOMO and LUMO of the $Na[BDSZ']^-$ model system. Interestingly, in this case the occupied orbital on the non-hydrogen-bonded sulfonate group is stabilized by the sodium and becomes energetically close to the bonding π -orbital on the nearby benzene ring. As a result, the HOMO is a superposition of orbitals on the non-hydrogen-bonded sulfonate group and this π -orbital. The HOMO–LUMO gap is 3.47 eV in this case and the vertical excitation energy is 3.14 eV. Obviously, the vertical excitation energy becomes larger the more the HOMO is stabilized by the cation, and this stabilization is larger for the alkali ions (Fig. 11) than for the proton (Fig. 8).

4.1.4 DFT results for $[Na_2-BDSZ]^{2-}$. For comparison, we have also studied the model system $[Na_2-BDSZ]^{2-}$, with four sulfonate groups and two sodium ions. In this case, we have only investigated the sodium analogue (not other alkali or proton adducts), assuming C_i symmetry. The model system is sketched in Fig. 12.

The HOMO and LUMO (not shown) are qualitatively very similar to the corresponding orbitals on the $[Na-BDSZ']^-$ model system. $[Na_2-BDSZ]^{2-}$ differs slightly from $[Na-BDSZ']^-$ in that its HOMO is localized somewhat more on the central chromophore system.

We can summarize our DFT results as follows: while the LUMOs are almost mutually indistinguishable for all the model systems, the HOMOs are quite different in the various systems and much more dependent on the interaction with the cation. In the $[Na_2-BDSZ]^{2-}$ system, the first singlet excited state is found at 3.33 eV (1A_u state). For the full system, $[M-BDSZ]^{3-}$, we expect that the two singlet excited states that are responsible for the tunneling described here are states that are obtained after exciting one electron from a sulfonate group at either side of the molecule to the common π -type LUMO. The excitation occurring at the side with the cation (M^+ or H^+) is distinct from the excitation occurring on the other, "empty" side and at lower energy relative to the latter excitation.

4.2 Dynamics versus energetics

We first refer the reader to the energy level diagram of Fig. 13 for the following discussion.

4.2.1 Kinetic model. Our experiments and calculations suggest the following picture. Isolated BDSZ-based trianions can resonantly absorb a photon over a wide UV wavelength range and then relax (by internal conversion) to a common long-lived lower excited state(s), from which ESETD occurs. Upon 388 nm excitation of $(M-BDSZ)^{3-}$ at room temperature,

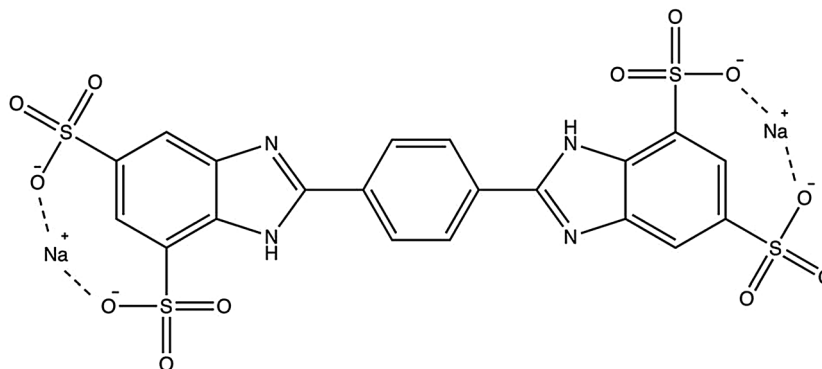


Fig. 12 The $[\text{Na}_2\text{-BDSZ}]^{2-}$ model system.

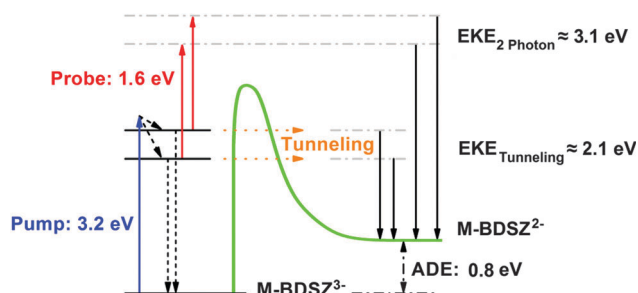


Fig. 13 Schematic energy level diagram with superimposed mechanistic steps of relevance for the observed TR-PES transients. Pump excitation at 3.2 eV leads to simultaneous population of two close-lying excited states at different electron tunneling rates. Both contribute to the tunneling signal at EKE \sim 2.1 eV. The population of these excited singlet states is probed by a second photon at 1.6 eV.

two different singlet excited states become simultaneously populated. Each has significant charge transfer character, involving transfer of electron density from the perimeter of the chromophore towards its center. The higher lying state of the two can decay more rapidly by ESETD because it is closer to the RCB top (where the barrier is correspondingly narrower). It is likely that both tunneling states are to some degree also coupled to the singlet ground state (*via* internal conversion and (slower) fluorescence). The fitted lifetimes τ_1 and τ_2 reflect a superposition of all of these decay processes. However, as Fig. 3 and Fig. S4 (ESI†) explicitly demonstrate for four of the trianions studied here, ESETD is the dominant decay process. We assume that this is also the case for the other M of interest in this study. Thus τ_1 and τ_2 provide a first order measure of the corresponding tunneling lifetimes. The systematic trend in τ_2 *vs.* alkali cation size can be rationalized by the corresponding transition energies as determined from theory (see below). The protonated system does not follow the trend because it has a different equilibrium structure type.

4.2.2 Vibrational excitation and electron tunnelling. Upon cooling both $[\text{H-BDSZ}]^{3-}$ and $[\text{Na-BDSZ}]^{3-}$ ions from room temperature to 20 K (Fig. S5, ESI†) we observe no significant change in the one-photon photoelectron spectra, in particular no change in the bandwidth of the tunneling feature. This suggests that any ground state vibrational cooling effects are

“swamped” by more significant structural relaxation induced by photoexcitation. We have not determined the corresponding tunneling lifetimes at 20 K (because the TR-PES experiment is presently set up only for room temperature operation). However, we do not expect them to be significantly different from room temperature for the same reason.

In a recent TR-PES study of excited state tunneling detachment from a (deprotonated) fluorescein dianion, the lifetime of the tunneling state was found to be essentially independent of excess vibrational excitation (*varied over a range of ca. 0.3 eV* by changing the pump laser wavelength).¹² The authors rationalized this in terms of an unexpectedly weak coupling of electronic and vibrational degrees of freedom. Such coupling depends on the extent to which the molecular topology changes with vibrational excitation and how this changes the transparency of the barrier surface – *on the timescale of the tunneling process*. On a timescale of <1 ps, the RCB barrier hypersurface of the fluorescein dianion apparently remains essentially the same throughout the vibrational excitation range studied. This in turn implies that the observed tunneling rate is significantly faster than the time required for excited state intramolecular vibrational energy redistribution (IVR) in this molecule.

In contrast to this, our observed trend in τ_2 values *vs.* the alkali cation size for $[\text{M-BDSZ}]^{3-}$ can be interpreted as indicating a *significant influence* of excess vibrational energy on the corresponding excited state lifetimes. In our calculations we find that the heavier the alkali, the lower the first singlet excited state energies (the protonated complex is an exception to this rule as its ground state structure differs from those of the other species). Consequently, fixed wavelength excitation at 388 nm leads to more excess vibrational energy in the respective excited state in the case of the heavier alkalis. This is apparently associated with faster tunneling decay. For $[\text{M-BDSZ}]^{3-}$, the observed tunnelling rates are in general smaller than the expected IVR rates. Consequently, as vibrational excitation is increased, significant changes in the effective RCB barrier surfaces could occur on a timescale fast enough to affect the tunnelling rates. Having said this, one must keep in mind that the alkali-dependent changes in ground state equilibrium geometry of the complexes (plus variations in polarizability of the complexed cations) can also lead to M-dependent changes

in “vibrationless” RCB surfaces. These might themselves lead to changes in ESETD rates. We hope that our observations will stimulate further theoretical treatment of ESETD in these systems.

5. Summary

We have observed constant electron kinetic energy features, in a series of BDSZ-derived trianions, $[M-BDSZ]^{3-}$ and $[BDSZ-SO_3 + H]^{3-}$, that are due to electron tunneling detachment from an excited state of the MCAs. We have probed the transient response associated with the constant kinetic energy features by time-resolved pump-probe photoelectron spectroscopy. The photoexcited trianions decay dominantly by delayed emission of electrons having kinetic energies consistent with tunneling detachment from the two lowest, close-lying, singlet excited states. Two-photon transients have been fit assuming parallel first order decay from these two states. The faster of the two rates is essentially constant for all trianions probed. The slower process is associated with lifetimes ranging from several picoseconds to tens of picoseconds depending on the complexed cation – with the lighter alkalis having systematically longer lifetimes. Quantum chemical calculations of excited state energies indicate that these differences are primarily a result of M-dependent shifts in transition energies which can in turn be rationalized in terms of corresponding geometry changes and their influence on charge transfer excitation, in particular on the HOMO energy. Fixed wavelength excitation leads to higher levels of vibrational excitation in those complexes with lower excited state energies – and correspondingly faster decay. This faster tunneling detachment may be associated with effective RCB narrowing due to the associated molecular distortion. Note that all excited state lifetimes measured in this study are significantly longer than the IVR randomization times expected upon electronic excitation of organic molecules in this size range.

UV excited BDSZ is known to undergo strong fluorescence in solution. The fluorescence quantum yields for gaseous $[M-BDSZ]^{3-}$ adducts are not known. However, in contrast to the significantly shorter lived photoexcited (deprotonated) fluorescein dianion and $[BDSZ]^{4-}$ systems, where we would not expect to be able to see gas-phase fluorescence,³² emission in $[M-BDSZ]^{3-}$ might be measurable in particular for those alkalis having the longest tunneling lifetimes. Together with ion depletion/photodissociation spectra to provide absorption cross sections this would then allow a more complete determination of branching ratios for the most important decay channels following optical excitation in these systems.

Acknowledgements

This work was supported by the Deutsche Forschungsgemeinschaft as administered: (i) by the Karlsruhe Excellence Cluster “Center for Functional Nanostructures (CFN)” – subproject C3.02 (MMK and ANU) and (ii) by the Transregio SFB TRR 88 “3MET” – subprojects C1 and C7 (WK, MK and MMK).

The experiments done at Brown were supported by the National Science Foundation (Grant No. CHE-1049717 to L.S.W.).

References

- 1 M. K. Scheller, R. N. Compton and L. S. Cederbaum, *Science*, 1995, **270**, 1160–1166.
- 2 L. S. Wang, C. F. Ding, X. B. Wang, J. B. Nicholas and B. Nicholas, *Phys. Rev. Lett.*, 1998, **81**, 2667–2670.
- 3 X. B. Wang, C. F. Ding and L. S. Wang, *Phys. Rev. Lett.*, 1998, **81**, 3351–3354.
- 4 X. B. Wang and L. S. Wang, *Annu. Rev. Phys. Chem.*, 2009, **60**, 105–126.
- 5 X. B. Wang and L. S. Wang, *Nature*, 1999, **400**, 245–248.
- 6 X. B. Wang, C. F. Ding and L. S. Wang, *Chem. Phys. Lett.*, 1999, **307**, 391–396.
- 7 X. B. Wang and L. S. Wang, *Phys. Rev. Lett.*, 1999, **83**, 3402–3405.
- 8 P. Weis, O. Hampe, S. Gilb and M. M. Kappes, *Chem. Phys. Lett.*, 2000, **321**, 426–432.
- 9 M. N. Blom, O. Hampe, S. Gilb, P. Weis and M. M. Kappes, *J. Chem. Phys.*, 2001, **115**, 3690–3697.
- 10 O. T. Ehrler, J. P. Yang, A. B. Sugiharto, A. N. Unterreiner and M. M. Kappes, *J. Chem. Phys.*, 2007, **127**, 184301.
- 11 P. D. Dau, H.-T. Liu, J.-P. Yang, M.-O. Winghart, T. J. A. Wolf, A.-N. Unterreiner, P. Weis, Y.-R. Miao, C.-G. Ning, M. M. Kappes and L.-S. Wang, *Phys. Rev. A*, 2012, **85**, 064503.
- 12 D. A. Horke, A. S. Chatterley and J. R. R. Verlet, *Phys. Rev. Lett.*, 2012, **108**, 083003.
- 13 D. A. Horke, A. S. Chatterley and J. R. R. Verlet, *J. Phys. Chem. Lett.*, 2012, **3**, 834–838.
- 14 X. B. Wang, K. Ferris and L. S. Wang, *J. Phys. Chem. A*, 2000, **104**, 25–33.
- 15 M. Kasha, *Discuss. Faraday Soc.*, 1950, **9**, 14–19.
- 16 L. S. Wang, C. F. Ding, X. B. Wang and S. E. Barlow, *Rev. Sci. Instrum.*, 1999, **70**, 1957–1966.
- 17 X. P. Xing, X. B. Wang and L. S. Wang, *J. Chem. Phys.*, 2009, **130**, 074301.
- 18 X. B. Wang and L. S. Wang, *Rev. Sci. Instrum.*, 2008, **79**, 073108.
- 19 P. D. Dau, H. T. Liu, D. L. Huang and L. S. Wang, *J. Chem. Phys.*, 2012, **137**, 116101.
- 20 O. T. Ehrler, *Ph.D. Thesis*, University of Karlsruhe (TH), 2006; C. Rensing, *Ph. D. Thesis*, KIT, 2010.
- 21 (a) V. Dribinski, A. Ossadtchi, V. A. Mandelshtam and H. Reisler, *Rev. Sci. Instrum.*, 2002, **73**, 2634–2642; (b) G. A. Garcia, L. Nahon and I. Powis, *Rev. Sci. Instrum.*, 2004, **75**, 4989–4996.
- 22 H.-T. Liu, Y.-L. Wang, X.-G. Xiong, P. D. Dau, Z. A. Piazza, D.-L. Huang, C.-Q. Xu, J. Li and L.-S. Wang, *Chem. Sci.*, 2012, **3**, 3286–3295.
- 23 (a) X. B. Wang and L. S. Wang, *J. Chem. Phys.*, 1999, **111**, 4497–4509; (b) J. Friedrich, S. Gilb, O. T. Ehrler, A. Behrendt and M. M. Kappes, *J. Chem. Phys.*, 2002, **117**, 2635–2644.
- 24 F. Furche and D. Rappoport, *Density functional methods for excited states: equilibrium structure and electronic spectra*,

- in *Computational Photochemistry*, ed. M. Olivucci, Elsevier, Amsterdam, vol. 16 of "Theoretical and Computational Chemistry", 2005.
- 25 A. D. Becke, *J. Chem. Phys.*, 1993, **98**, 5648–5652.
- 26 D. Rappoport and F. Furche, *J. Chem. Phys.*, 2010, **133**, 134105.
- 27 J. Simons, *J. Phys. Chem. A*, 2008, **112**, 6401–6511.
- 28 Turbomole V6.4 2012, a development of Universität Karlsruhe (TH) and Forschungszentrum Karlsruhe GmbH, 1989–2007, TURBOMOLE GmbH, since 2007. See <http://www.turbomole.com>, Karlsruhe.
- 29 See for example: K. Matheis, A. Eichhofer, F. Weigend, O. T. Ehrler, O. Hampe and M. M. Kappes, *J. Phys. Chem. C*, 2012, **116**, 13800–13809; M. Vonderach, O. T. Ehrler, K. Matheis, P. Weis and M. Kappes, *J. Am. Chem. Soc.*, 2012, **134**, 7830–7841.
- 30 S. Feuerbacher and L. S. Cederbaum, *J. Phys. Chem. A*, 2005, **109**, 11401–11406.
- 31 (a) A. Dreuw and M. Head-Gordon, *J. Am. Chem. Soc.*, 2004, **126**, 4007–4016; (b) A. Dreuw and M. Head-Gordon, *Chem. Rev.*, 2005, **105**, 4009–4037.
- 32 M. Kordel, D. Schooss, C. Neiss, L. Walter and M. M. Kappes, *J. Phys. Chem. A*, 2010, **114**, 5509–5514.